Available online at www.sciencedirect.com
ScienceDirect
Optics and Lasers in Engineering 45 (2007) 304–317
OPTICS and LASERS in ENGINEERING

Two-dimensional windowed Fourier transform for fringe pattern analysis: Principles, applications and implementations

Qian Kemao

School of Computer Engineering, Nanyang Technological University, Singapore 639798, Singapore

Abstract

Fringe patterns from optical metrology systems need to be demodulated to get the desired parameters. Two-dimensional windowed Fourier transform is chosen for the determination of phase and phase derivatives. Two algorithms, one based on filtering and the other based on similarity measure, are developed. Some applications based on these two algorithms are explored, including strain determination, phase unwrapping, phase-shifter calibration, fault detection, edge detection and fringe segmentation. Various examples are given to demonstrate the ideas. Finally implementations of these algorithms are addressed. Most of the work has appeared in various papers and its originality is not claimed. Instead, this paper gives an overview and more insights of our work on windowed Fourier transform.

Keywords: Windowed Fourier transform; Fringe demodulation; Optical metrology; Noise reduction; Strain; Phase unwrapping; Phase-shifter calibration; Fault detection; Edge detection; Fringe segmentation

1. Introduction

In optical metrology, the output is usually in the form of a fringe pattern, which should be further analyzed [1–4]. For example, phase retrieval from fringe patterns is often required. Two traditional techniques for phase retrieval are phase-shifting technique [1,5] and carrier technique with Fourier transform [1,6]. Phase-shifting technique processes the fringe patterns pixel by pixel. Each pixel is processed separately and does not influence the others. However, this technique is sensitive to noise. As an example, Fig. 1(a) shows one of four phase-shifted fringe patterns. Phase extracted using phase-shifting algorithm is shown in Fig. 1(b), which is obviously very noisy. On the contrary, carrier technique with Fourier transform processes the whole frame of a fringe pattern at the same time. It is more tolerant to noise, but pixels will influence each other. As an example, A carrier fringe pattern and its phase extracted using Fourier transform are shown in Fig. 2(a) and (b), respectively. A better result, if possible, is expected.

Thus a compromise between the pixel-wise processing and global processing is necessary. A natural solution is to process the fringe patterns locally, or block by block. A smoothing filter is a typical local processor [7]. It assumes that the intensity values in a small block around each pixel (u, v) are the same and hence the average value of that block is taken as the value of pixel (u, v). Obviously it is not reasonable for a fringe pattern since its intensity undulates as a cosine function (see next paragraph). Because of this, more advanced and effective techniques, such as regularized phase tracking (RPT) [4,8–12], wavelet transform [13–23], Wigner–Ville distribution [19,24] and windowed Fourier transform (WFT) [19,25,26], were proposed. In this paper, principle of WFT will be emphasized and compared with other techniques. Then various applications of WFT and the implementation issues will be introduced. Figs. 1(c) and 2(c) show the effectiveness of WFT at a first glance. Again it is emphasized that most of the work has appeared in various papers and its originality is not claimed. Instead, this paper gives an overview and more insights of our work on WFT.

Before further discussion, a brief definition and analysis of fringe patterns are given, which will be used throughout the paper. A fringe pattern can be generally expressed as

$$f(x, y) = a(x, y) + b(x, y)\cos[\varphi(x, y)], \tag{1}$$

E-mail address: mkmqian@ntu.edu.sg.

0143-8166/$ - see front matter © 2006 Elsevier Ltd. All rights reserved.
doi:10.1016/j.optlaseng.2005.10.012

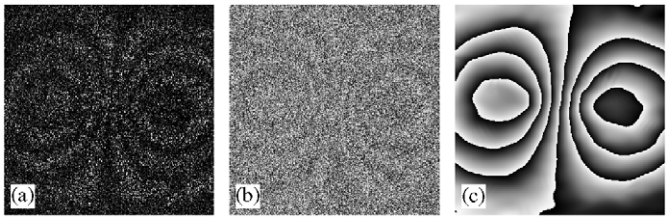

Fig. 1. Phase retrieval from phase-shifted fringes: (a) one of four phase-shifted fringe patterns; (b) phase by phase-shifting technique and (c) phase by windowed Fourier transform.

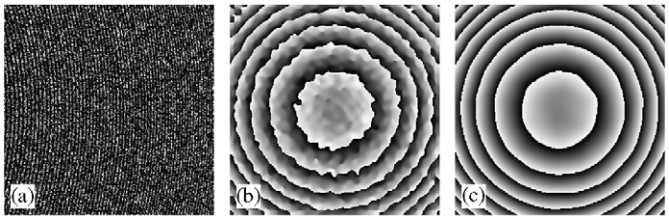

Fig. 2. Phase retrieval from a carrier fringe: (a) a carrier fringe pattern; (b) phase by Fourier transform and (c) phase by windowed Fourier transform.

where $f(x,y)$, $a(x,y)$, $b(x,y)$ and $\varphi(x,y)$ are the recorded intensity, background intensity, fringe amplitude and phase distribution, respectively. Fringe patterns are classified into four types: (I) exponential phase fringe patterns, (II) wrapped phase fringe patterns, (III) carrier fringe patterns and (IV) closed fringe patterns. Exponential phase fringe patterns, which are analytic signals, are fundamental for fringe processing [27] and are basic patterns considered in this paper. They can be obtained from, say, phase shifting technique. For example, given four phase-shifted fringe patterns as

$$f_i(x,y) = a(x,y) + b(x,y)\cos[\varphi(x,y) + (i-1)\pi/2], \quad i = 1,2,3,4,$$

the combination of $\frac{1}{2}[f_1(x,y) - f_3(x,y) + \mathrm{j}f_4(x,y) - \mathrm{j}f_2(x,y)]$ gives

$$f_{\mathrm{I}}(x,y) = b(x,y)\exp[\mathrm{j}\varphi(x,y)], \tag{2}$$

where $\mathrm{j} = \sqrt{-1}$. The phase can be obtained by taking the angle of $f_{\mathrm{I}}(x,y)$, which is usually very noisy. Sometimes wrapped phase maps are given. A typical example is phase unwrapping. This type of fringe patterns can be written as

$$f_{\mathrm{II}}(x,y) = \varphi_{\mathrm{w}}(x,y), \tag{3}$$

where $\varphi_{\mathrm{w}}(x,y)$ denotes a wrapped phase map. It can be easily converted to f_{I} by simply multiplying it with j and taking its exponential value. In this paper, f_{II} is always converted to f_{I} before any processing. The third type, carrier fringe patterns, can be written as

$$f_{\mathrm{III}}(x,y) = a(x,y) + b(x,y) \times \cos[\omega_{\mathrm{c}x}x + \omega_{\mathrm{c}y}y + \varphi(x,y)], \tag{4}$$

where $\omega_{\mathrm{c}x}$ and $\omega_{\mathrm{c}y}$ are carrier frequencies along x and y directions, respectively. They are usually constants. Since $\cos(t) = \exp(\mathrm{j}t)/2 + \exp(-\mathrm{j}t)/2$, f_{III} consists of a background field and two conjugated fringe patterns of f_{I}. These three items are separable in Fourier domain provided that the carrier frequencies are high enough. Thus, it can also be converted to f_{I}. However, this conversion is unnecessary as the separation is realized automatically in the WFT algorithms. The fourth type, closed fringe patterns, can be written as

$$f_{\mathrm{IV}}(x,y) = a(x,y) + b(x,y)\cos[\varphi(x,y)]. \tag{5}$$

It also consists of a background field and two conjugated fringe patterns of f_{I}, but they are not separable. Thus converting f_{IV} to f_{I} is generally not easy. Other cues, such as a fringe follower [12] or fringe orientation [28], are required. Note that though the expressions of Eqs. (1) and (5) are the same, the former refers to general fringe patterns while the latter refers to f_{IV}.

Local frequencies (or instantaneous frequencies) are used to express phase derivatives as

$$\omega_x(x,y) = \frac{\partial\varphi(x,y)}{\partial x}, \tag{6}$$

$$\omega_y(x,y) = \frac{\partial\varphi(x,y)}{\partial y}. \tag{7}$$

Phase distribution in a block around a pixel (u,v) can thus be approximated as a small plane,

$$\varphi(x,y) \approx \omega_x(u,v)(x-u) + \omega_y(u,v)(y-v) + \varphi(u,v). \tag{8}$$

For f_{III}, the carrier frequencies are usually included into the local frequencies. Note that there is slight difference in the definition of instantaneous frequencies [29]. Also note that in this paper, (x,y) and (u,v) are sometimes used interchangeably if no confusion is raised.

2. Principles of windowed Fourier transform

In this section, the WFT is first introduced, based on which, two algorithms, windowed Fourier filtering (WFF) and windowed Fourier ridges (WFR) are developed and discussed. To process the fringe patterns block by block, the WFT is by default two-dimensional (2-D) throughout this paper.

2.1. Windowed Fourier transform

The WFT and inverse WFT (IWFT) are a pair of transforms [25,29] as

$$Sf(u,v,\xi,\eta) = \int_{-\infty}^{\infty}\int_{-\infty}^{\infty} f(x,y)g^*_{u,v,\xi,\eta}(x,y)\,\mathrm{d}x\,\mathrm{d}y, \tag{9}$$

$$f(x,y) = \frac{1}{4\pi^2}\int_{-\infty}^{\infty}\int_{-\infty}^{\infty}\int_{-\infty}^{\infty}\int_{-\infty}^{\infty} Sf(u,v,\xi,\eta) \times g_{u,v,\xi,\eta}(x,y)\,\mathrm{d}\xi\,\mathrm{d}\eta\,\mathrm{d}u\,\mathrm{d}v, \tag{10}$$

where the symbol $*$ denotes the complex conjugate operation. Eq. (9) deconstructs a 2-D image $f(x,y)$ onto

WFT basis $g_{u,v,\xi,\eta}(x,y)$, resulting in 4-D coefficients (or WFT spectrum) $Sf(u,v,\xi,\eta)$, while Eq. (10) reconstructs the image. The WFT basis consists of a series of windowed Fourier elements (or building blocks, atomic functions) as

$$g_{u,v,\xi,\eta}(x,y) = g(x-u,y-v)\exp(\mathrm{j}\xi x + \mathrm{j}\eta y). \tag{11}$$

Compared with the Fourier basis $\exp(\mathrm{j}\xi x + \mathrm{j}\eta y)$, which has an infinite spatial extension [30,31], WFT element has a limited spatial extension due to the window function $g(x-u,y-v)$. Consequently, the WFT spectrum, $Sf(u,v,\xi,\eta)$, gives the frequency information at each pixel in the image, which is impossible for Fourier transform. The cost is that WFT computation is heavier because its basis is redundant and not orthogonal [29]. WFT is also known as short-time Fourier transform [29]. It is also called Gabor transform if $g(x,y)$ is a Gaussian function given as [32]

$$g(x,y) = \exp[-x^2/2\sigma_x^2 - y^2/2\sigma_y^2], \tag{12}$$

where σ_x and σ_y are the standard deviations of the Gaussian function in x and y directions, respectively, which control the spatial extension of $g(x,y)$. A Gaussian window is often chosen as it provides the smallest Heisenberg box [29,32], which is useful in, for example, multispectral estimation [29]. The Gaussian window is selected throughout this paper, although a simple square window also works quite well. The Gaussian window function is divided by $\sqrt{\pi\sigma_x\sigma_y}$ for normalization such that $||g(x,y)||_2 = 1$.

2.2. Windowed Fourier filtering

The similarity of WFT and Fourier transform reminds us to filter a fringe pattern by processing its WFT spectrum [31]. The scheme is shown in Fig. 3. A fringe pattern is transformed into its spectrum. Generally the noise permeates the whole spectrum domain with very small coefficients due to its randomness and incoherence with the WFT basis. Thus it can be suppressed by discarding the spectrum coefficients if their amplitudes are smaller than a preset threshold. A smooth image is produced after an IWFT. The scheme can be expressed as

$$\bar{f}(x,y) = \frac{1}{4\pi^2}\int_{-\infty}^{\infty}\int_{-\infty}^{\infty}\int_{\eta_\mathrm{l}}^{\eta_\mathrm{h}}\int_{\xi_\mathrm{l}}^{\xi_\mathrm{h}} \overline{Sf}(u,v,\xi,\eta) \times g_{u,v,\xi,\eta}(x,y)\,\mathrm{d}\xi\,\mathrm{d}\eta\,\mathrm{d}u\,\mathrm{d}v \tag{13}$$

with

$$\overline{Sf}(u,v,\xi,\eta) = \begin{cases} Sf(u,v,\xi,\eta) \\ \quad \text{if} \quad |Sf(u,v,\xi,\eta)| \geqslant \mathrm{thr}, \\ 0 \\ \quad \text{if} \quad |Sf(u,v,\xi,\eta)| < \mathrm{thr}, \end{cases} \tag{14}$$

where $\overline{Sf}(u,v,\xi,\eta)$ denotes the thresholded spectrum and $\bar{f}(x,y)$ denotes the filtered fringe pattern; 'thr' denotes the threshold. The WFF can be applied to all the four types of fringe patterns. For f_{III}, if only the spectrum of one side-lobe around the carrier frequencies is selected, WFF gives an exponential field, from which phase can be extracted [33]. This is similar to the traditional Fourier transform technique for demodulation of carrier fringe patterns [6]. For f_{IV}, if the spectrum of all the possible frequencies is selected, WFF gives a filtered fringe pattern. The output is usually a complex field and its real part should be used. If either ξ or η is enforced to be positive, then WFF gives an exponential phase field. Its angle gives an ambiguous phase distribution [26]. This is similar to Kreis' approach [34]. When the phase is obtained, local frequencies can be obtained according to Eqs. (6) and (7) [35].

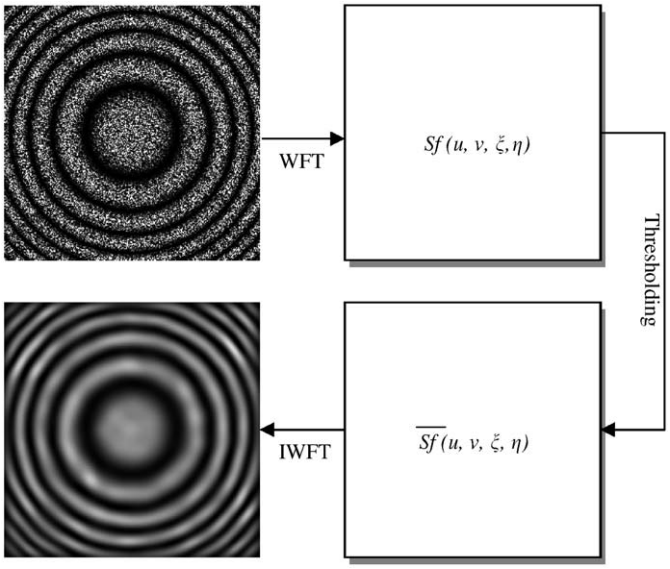

Fig. 3. Scheme of WFF. The input is a noisy fringe pattern and the output is a filtered fringe pattern.

Note that instead of from $-\infty$ to ∞, the integration limits in Eq. (13) are set to be from ξ_l to ξ_h and from η_l to η_h for ξ and η, respectively. This means that only the spectrum of $[\xi,\eta] \in [\xi_\mathrm{l},\xi_\mathrm{h}] \times [\eta_\mathrm{l},\eta_\mathrm{h}]$ should be computed if the frequencies of the fringe pattern are known to be in this range. It is unnecessary to compute other coefficients and thus the computational cost is saved. The range can be estimated by analyzing the density or Fourier spectrum of a fringe pattern. If the useful frequency components are estimated as $[\xi,\eta] \in [a,b] \times [c,d]$, then the range for WFF is expanded as $[\xi,\eta] \in [a-3/\sigma_x, b+3/\sigma_x] \times [c-3/\sigma_y, d+3/\sigma_y]$. The reason for the expansion is as follows. For a signal with frequencies of $[\xi_0,\eta_0]$ around (u,v), due to the Gaussian window function, its WFT spectrum $Sf(u,v,\xi,\eta)$ extends infinitely along ξ and η axes. However, 99.5% of energy is concentrated in $[\xi_0-3/\sigma_x, \xi_0+3/\sigma_x] \times [\eta_0-3/\sigma_y, \eta_0+3/\sigma_y]$. An expansion of $\pm 2/\sigma_x$ and $\pm 2/\sigma_y$ can be practically selected. This expansion is necessary for recovering the image accurately through IWFT.

2.3. Windowed Fourier ridges

WFR is another algorithm to process fringe patterns. Consider only a small block of a fringe pattern around a pixel (u,v) and compare it with a WFT element $g_{u,v,\xi,\eta}(x,y)$. The values of ξ and η are continuously changed. There exists one WFT element that gives the highest similarity, which is usually referred to as a ridge [29,36,37]. The values of ξ and η that maximize the similarity are taken as the local frequencies at pixel (u,v). Local frequencies for all the pixels can be estimated by sliding the block. The WFR scheme is illustrated in Fig. 4. Since the similarity can be represented by spectrum amplitude, it can thus be expressed as

$$[\omega_x(u,v),\omega_y(u,v)] = \arg\max_{\xi,\eta} |Sf(u,v,\xi,\eta)| \tag{15}$$

which means that $\omega_x(u,v)$ and $\omega_y(u,v)$ take the value of ξ and η, respectively, when these values maximize the amplitude spectrum $|Sf(u,v,\xi,\eta)|$. The ridge and phase values are consequently determined as follows [25]:

$$r(u,v) = |Sf[u,v,\omega_x(u,v),\omega_y(u,v)]|, \tag{16}$$

$$\varphi(u,v) = \text{angle}\{Sf[u,v,\omega_x(u,v),\omega_y(u,v)]\} + \omega_x(u,v)u + \omega_y(u,v)v. \tag{17}$$

The phase is wrapped and phase unwrapping is necessary. This is called *phase from ridges* [25]. The phase can be obtained in another way. Since $\omega_x(u,v)$ and $\omega_y(u,v)$ are obtained, the phase can be computed by integrating them. This is called *phase by integration* [25]. Both of them have limitations. For the *phase from ridges*, when the window size is not very small, say $\sigma_x = \sigma_y = 10$, the phase should be corrected by

$$-\tfrac{1}{2}\arctan[\sigma_x^2\varphi_{xx}(u,v)] - \tfrac{1}{2}\arctan[\sigma_y^2\varphi_{yy}(u,v)],$$

where $\varphi_{xx}(u,v) = \partial^2\varphi/\partial x^2$ and $\varphi_{yy}(u,v) = \partial^2\varphi/\partial y^2$ are second-order derivatives. On the other hand, for the *phase by integration*, when $\omega_x(u,v)$ and $\omega_y(u,v)$ are integrated, their errors are also accumulated, which might lead to a large phase error [25]. Finally, in order to save time, the possible frequencies could be tested within an estimated range of $[\xi,\eta] \in [\xi_l,\xi_h] \times [\eta_l,\eta_h]$. Unlike the WFF, no expansion is needed since IWFT is not involved. The WFR can be applied to all the four types of fringe patterns. For f_{IV}, the local frequencies and phase distribution are ambiguous, due to the fact that if $\omega_x(u,v)$, $\omega_y(u,v)$ and $\varphi(u,v)$ is a solution, so is $-\omega_x(u,v)$, $-\omega_y(u,v)$ and $-\varphi(u,v)$. An example is shown in Fig. 4.

2.4. Comparison with other techniques

WFF and WFR are compared with other techniques to clarify their similarities and differences, which would be helpful for proper use of these techniques.

2.4.1. WFF vs. Fourier and orthogonal wavelet filtering

The WFF scheme is very similar to Fourier transform denoising [31] and discrete wavelet transform denoising [38,39]. The main difference is the transform bases. WFT usually gives better noise reduction effects due to the following reasons. Firstly, WFT basis has higher coherence to the fringe patterns. As can be seen from Eqs. (2)–(5), a fringe pattern basically consists of one (f_I and f_{II}) or two (f_{III} and f_{IV}) exponential phase fields. Since the phase in each local area can be approximated by a plane, the fringe pattern can be well represented by a WFT element, resulting in sparse and large spectrum coefficients. This representation is easier for further processing. For example, a simple thresholding proposed in this paper usually gives good results. Secondly, when the spectrum is thresholded, the useful information might also be slightly destroyed. As a redundant basis, WFT is more tolerant to the disturbance of spectrum [29,40,41].

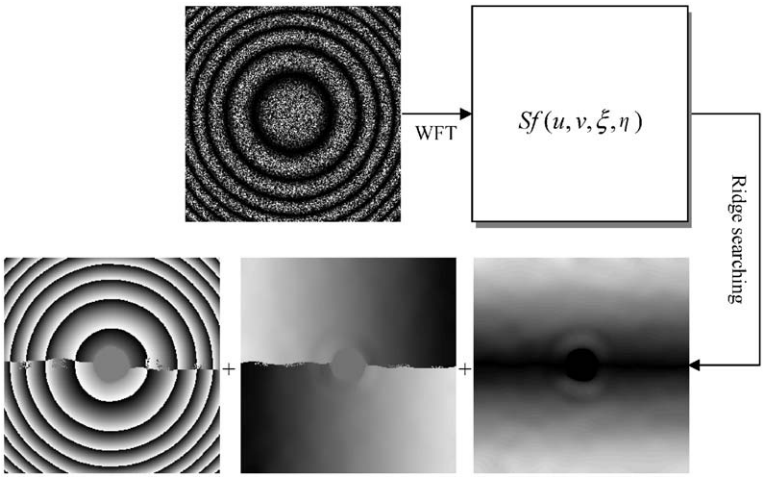

Fig. 4. Scheme of WFR. The input is a noisy fringe pattern, the output (from left to right) are phase distribution and local frequencies in x and y directions, respectively. In this illustration, as an example, a closed fringe pattern is taken as the input, consequently sign ambiguities are observed in the output.

2.4.2. WFR vs. RPT

The WFR is similar to the RPT in their basic principles. The RPT constructs different cosine elements as

$$g^{\mathrm{RPT}}_{u,v,\xi,\eta,\varphi}(x,y) = g(x-u,y-v)\cos[\xi x+\eta y+\varphi(u,v)] \quad (18)$$

and looks for the most similar one to the fringe pattern in each local area. It is basically used for f_{IV} [8], but can be easily extended to process f_{I} [9], f_{II} [10] and f_{III} [11]. The cosine elements of RPT can be deconstructed into two conjugated exponential elements, i.e., two WFT elements. Hence WFT elements are more fundamental than RPT elements. For WFR, all the possible combinations of ξ and η can be tested and the best WFT element for each local area can be found; but for RPT, three variables, ξ, η and φ need to be estimated simultaneously. Testing all the possible combinations is impractical and hence an optimization strategy is necessary. Due to the success of RPT in f_{IV} demodulation, it would be interesting to explore the possibility of using WFR to demodulate f_{IV} automatically without phase ambiguity.

2.4.3. WFR vs. wavelet ridges

Wavelet transform is another popular approach for phase retrieval [13–23]. The Gabor wavelet (or Morlet wavelet) is most often used. It can be written as

$$g^{\mathrm{Wavelet2D}}_{u,v,\xi,\eta}(x,y) = g\left[\frac{(x-u)\xi}{\xi_0},\frac{(y-v)\eta}{\eta_0}\right] \times \exp(\mathrm{j}\xi x+\mathrm{j}\eta y), \quad (19)$$

where ξ_0 and η_0 are the preset constants. Compared with Eq. (11), it can be seen that the only difference of wavelet basis and WFT basis is the window size. For WFT basis, the window size is fixed, while for wavelet basis, it is variable. The window size increases when frequency ξ or η decreases. Thus, it is troublesome in processing fringe patterns with very low frequencies. For example, for the carrier fringe pattern shown in Fig. 2(a), the frequency of the fringe pattern along y direction is extremely low, which requires the window size of wavelet along y direction to be nearly infinite. Thus it is not practical to construct a 2-D wavelet and perform a 2-D continuous wavelet transform. Instead, the fringe patterns are often processed row by row through 1-D wavelet transform with following wavelet basis:

$$g^{\mathrm{Wavelet1D}}_{u,\xi}(x) = g\left[\frac{(x-u)\xi}{\xi_0}\right]\exp(\mathrm{j}\xi x). \quad (20)$$

But this introduces another problem. Fig. 5(a) shows the central row of Fig. 2(a). Its structure can hardly be discriminated. Consequently, the result by 1-D wavelet transform is not as good as that by WFT [25]. As an example, a noiseless version of carrier fringe pattern corresponding to Fig. 2(a) is simulated. Both noiseless and noisy carrier fringe pattern are processed using the technique of 1-D wavelet ridges and the phase distributions are shown in Fig. 5(b) and (c), respectively. It is obvious

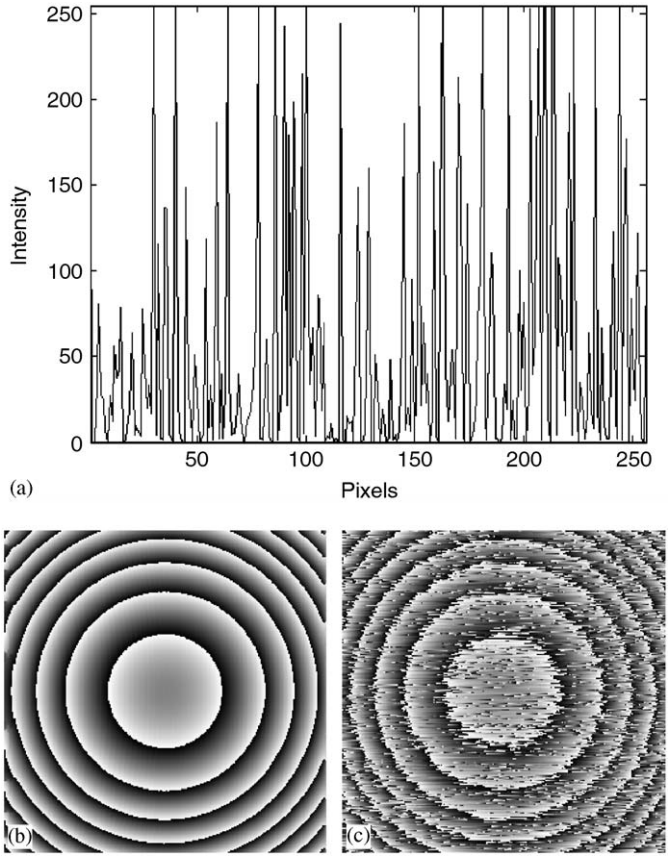

Fig. 5. Technique of 1-D wavelet ridges: (a) The central row of Fig. 2(a). The structure of the fringe pattern can hardly be observed; (b) retrieved phase distribution when the fringe pattern is noiseless and (c) Retrieved phase distribution when fringe pattern is noisy. The noisy fringe pattern is same as Fig. 2(a).

that 1-D wavelet transform is quite sensitive to noise. For this reason, wavelet is often used in dynamic problems where the signals are 1-D [22,23], or in fringe projection profilometry [20,21] and moiré interferometry [15,16] where the fringe patterns are less noisy.

As wavelet automatically changes the window size, WFT is often criticized that it has to fix the window size and is not adaptive to the fringe pattern. However this is rather misleading. The following comments by Laine are more reasonable. 'If the signal consists mostly of time-harmonic components, which, even at high frequencies, have a long correlation time, then a windowed Fourier transform, with building blocks that share these characteristics, is best. If the signal consists of a wide range of frequencies, with much shorter correlation times for the high frequencies than for the low frequencies (which is typically the case with transients superposed on more slowly changing components or short-lived transients between smoother parts of the signal), then the "zoom-in" quality of the wavelet transform is more useful, because it has a very small field of vision for high frequencies but can be used to view low frequencies at a larger scale.' [42]. It is assumed that for a natural scene, low-frequency components usually

last for long durations while high-frequency components usually last for short durations, which is suitable to be analyzed using wavelet. However, this assumption is obviously not reasonable for the fringe patterns. For example, a typical fringe pattern shown as the input of Figs. 3 and 4 has same duration for all the frequency components. It is fair to have a fixed window size. Further, recall that a fringe pattern is either an exponential field or a cosine function with its phase locally approximated by Eq. (8). For each pixel (u, v), only three unknowns, $\omega_x(u, v)$, $\omega_y(u, v)$ and $\varphi(u, v)$, need to be determined. For noiseless fringe patterns, they can be accurately recovered in either a small window or a large window, regardless of the value of frequencies. A small window reduces the approximation error while a large window is more robust against noises. According to our experience, $\sigma_x = \sigma_y = 10$ gives good results. It is emphasized that the choice of window size is based on a trade-off between accuracy of phase approximation and immunity to noise, instead of on the duration of frequency components of a fringe pattern.

2.4.4. WFR vs. Gabor filters and wavelets for texture analysis

Gabor filters were proposed by Bovik et al. [43] for texture analysis, where the texture is assumed to be a cosine function. Though this assumption is somewhat idealized, they argued that "the global is to *segment* images based on texture, rather than to form a complete description of the textures" [43]. To deal with emergent image frequencies in nonstationary signals, they turned to Gabor wavelets [44]. As mentioned in Section 2.4.3, a fringe pattern is either an exponential field or a cosine function, which can be suitably processed by WFR. Further, accurate local frequency and phase retrieval, as a complete description of a fringe pattern, is required and always emphasized in WFR due to its high importance in metrology, which is different from texture analysis. Though WFR can be seen as a simple and special case of Gabor filters, different motivations lead to different algorithms.

3. Applications of WFT

3.1. Phase and frequency retrieval by WFF and WFR

It can be seen from Section 2 that the phase distribution and local frequencies can be extracted. Figs. 1(c) and 2(c) show two examples, which can be obtained by either WFF or WFR with very similar results. The functions of WFF and WFR are illustrated in Figs. 6 and 7. Suggestion for the selection of frequency ranges is given in Table 1. Following are some notations.

(1) The accuracy of WFF and WFR for f_{I}, f_{II} and f_{III} was investigated in Ref. [25]. It is typically below one fiftieth of a wavelength for both WFF and WFR.
(2) The accuracy of WFF for f_{IV} was investigated in Ref. [41]. The relative error is 11% for speckle noise.

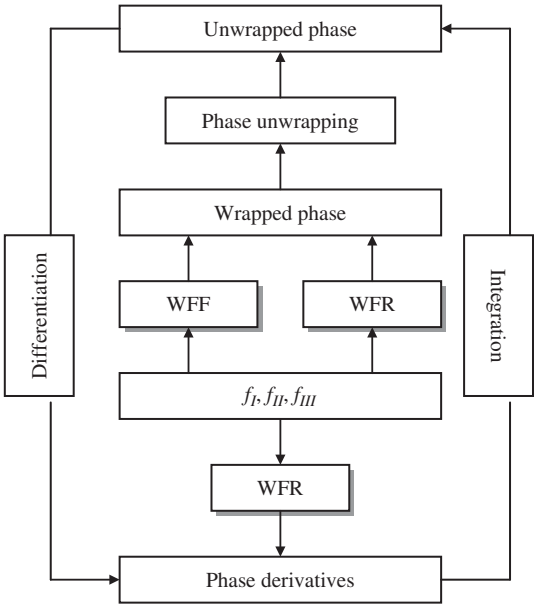

Fig. 6. WFF and WFR for f_{I}, f_{II} and f_{III}.

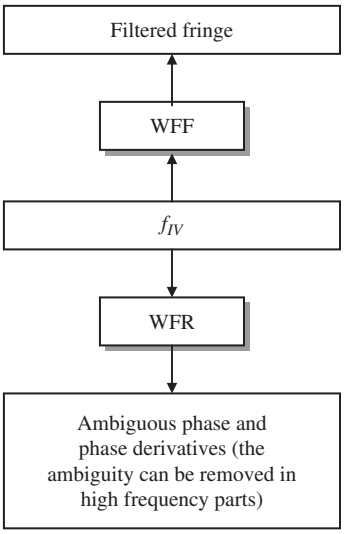

Fig. 7. WFF and WFR for f_{IV}.

(3) The accuracy of WFR for f_{IV} was investigated in Ref. [26]. The background of $a(x, y)$ should be removed from f_{IV} before WFR is applied to f_{IV}. The accuracy of both phase and phase derivatives are high at high-frequency parts, while they are low at low-frequency parts. This gives a hint that at least some parts of f_{IV} can be accurately demodulated. However, whether a frequency is high or low is rather subjective. A guideline is that in a local area, $b(x, y)\exp[\mathrm{j}\varphi(x, y)]$ and $b(x, y)\exp[-\mathrm{j}\varphi(x, y)]$ do not overlap in the frequency domain. For a Gaussian window function with $\sigma_x = \sigma_y$, empirically a high local frequency should at least satisfy $\omega = \sqrt{\omega_x^2 + \omega_y^2} \geqslant 1.5/\sigma_x$.

Table 1
Selection of the frequency region

Input	Algorithms	ξ_l	ξ_h	η_l	η_h	Examples[a]
f_I	WFF and WFR	<0	>0	<0	>0	Fig. 1, $[-0.5,0.5]\times[-0.5,0.5]$
f_{III}	WFF and WFR	$<\omega_{cx}$	$>\omega_{cx}$	$<\omega_{cy}$	$>\omega_{cy}$	Fig. 2, $[-0.2,0.2]\times[1.0,2.1]$
f_{IV}	WFF	<0	>0	<0	>0	Fig. 3, $[-0.5,0.5]\times[-0.5,0.5]$
f_{IV}	WFR	$=0$ <0	>0 >0	<0 $=0$	>0 >0	Fig. 4, $[0,0.5]\times[-0.5,0.5]$

[a](1) Image size of examples: 256×256; (2) the coordinate is in MATLAB® convention and (3) all the regions given are based on WFR. Additional region expansion is needed for WFF.

(4) As WFF and WFR are local processors, the accuracy of the results around image borders is low due to border effects, though sometimes it is tolerable.
(5) WFF is usually faster than WFR, as will be mentioned in Section 4.
(6) Generally speaking, for phase retrieval, WFF is preferred for f_I, f_{II} and f_{III} while WFR is preferred for f_{IV}. For local frequency retrieval, WFR is preferred. However, for each practical problem, both algorithms can be attempted and compared.

Here demodulation of a single closed fringe pattern will be discussed a little further. As mentioned previously, when WFR is applied to f_{IV}, both local frequencies and phase distribution are ambiguous, which can be observed in Fig. 4 and is also shown in Fig. 8(a). The phase ambiguity of the high-frequency parts can be easily removed by enforcing the continuity of local frequencies. In detail, consider a pixel (u,v) as initial pixel. For its adjacent pixel, say, $(u+1,v)$, if

$$\begin{aligned}&|\omega_x(u+1,v)-\omega_x(u,v)|+|\omega_y(u+1,v)-\omega_y(u,v)|\\&\quad\leqslant|\omega_x(u+1,v)+\omega_x(u,v)|\\&\qquad+|\omega_y(u+1,v)+\omega_y(u,v)|,\end{aligned}$$

take $\omega_x(u+1,v)$, $\omega_y(u+1,v)$ and $\varphi(u+1,v)$ as the solution; otherwise change their signs. Other pixels are processed in the same manner. Fig. 8(b) shows the phase of Fig. 8(a) with phase ambiguity removed. Finally, the low-frequency part can be filled using RPT, as shown in Fig. 8(c). One more example is shown in Fig. 9 which contains a saddle point. The phases are obtained in the same way. Further, in recently proposed techniques for demodulation of a single fringe pattern, WFR can serve as an initialization for refinement and propagation [45] while WFF can serve as an effective filtering method in extreme map based approach [46].

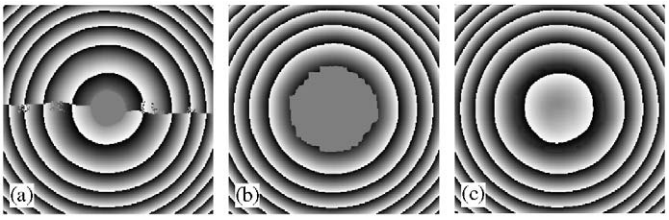

Fig. 8. Removal of phase ambiguity in a close fringe pattern: (a) phase from WFR that is reprinted from Fig. 4; (b) phase ambiguity is removed in the high-frequency part and (c) The low-frequency part is filled using RPT.

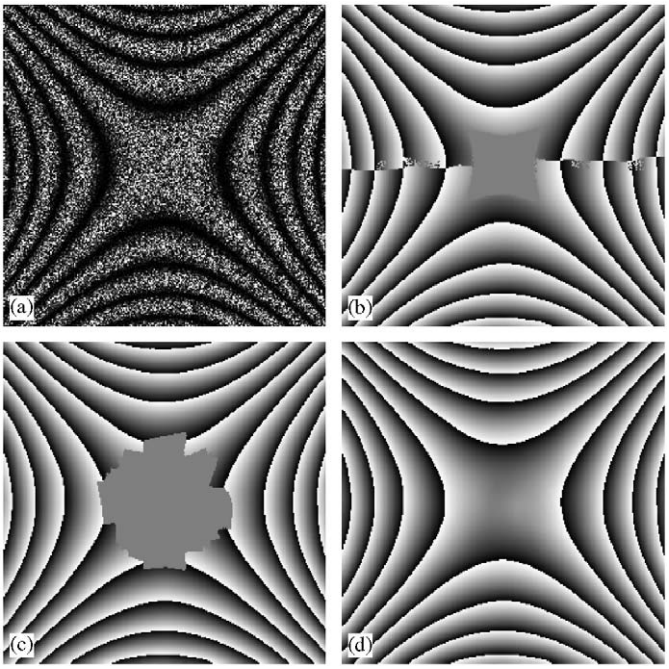

Fig. 9. Demodulation of a single fringe pattern: (a) the original fringe pattern; (b) phase from WFR; (c) phase ambiguity is removed in the high-frequency part and (d) The low-frequency part is filled using RPT.

3.2. Strain estimation in moiré interferometry

Though strains in moiré interferometry and local frequencies (instantaneous frequencies) in image processing are different concepts in mechanics and signal communication, it was recognized that they are the same except for a constant [18]. Thus strain can be estimated through local frequency extraction from moiré interferograms using

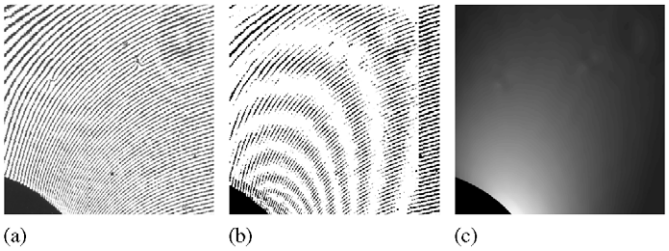

Fig. 10. WFR for strain extraction: (a) a moiré fringe pattern; (b) strain contour in x direction using moiré of moiré technique and (c) strain field by WFR.

WFF or WFR. It is a trivial extension of the application in Section 3.1. A real fringe moiré pattern (Fig. 10(a)) is processed as an example. The strain contour can be produced using moiré of moiré technique [47]. It is obtained by shifting the moiré fringe and overlapping it with the original one, which is shown in Fig. 10(b). The strain in x direction using WFR is given in Fig. 10(c), which provides the whole field information with good quality.

3.3. Phase unwrapping

Phase unwrapping is frequently needed to construct a continuous phase map $\varphi(x,y)$ from a wrapped phase map $\varphi_w(x,y)$ [48]. The only difference between $\varphi(x,y)$ and $\varphi_w(x,y)$ is 2π jumps. Hence, the phase can be unwrapped by scanning the phase map line by line and compensating the jumps [49]. However this method is usually unsuccessful when applied to a noisy wrapped phase map (Fig. 11(a)). Two widely used strategies to overcome the problem are circumventing the "bad" pixels and approximating the phase in a least-squares sense [50]. A third strategy is to remove the noise before phase unwrapping, which can be effectively fulfilled by WFF [50]. Fig. 11(b) is the wrapped phase filtered by WFF, from which the phase unwrapping becomes trivial, as shown in Fig. 11(c).

Sometimes not only "bad" pixels but also "bad" regions, such as shown in Fig. 12(a), need to be handled. This problem can again be solved by WFF. Recall that wrapped phase f_{II} is first converted to an exponential field f_I, which has a unit amplitude. Since the spectrum in the "bad" regions is usually broader than in other places, more energy will be removed in WFF and the amplitude of the filtered exponential field, $|\bar{f}_I|$, becomes smaller. This can be seen from Fig. 12(b), which shows the amplitude of the filtered exponential field of Fig. 12(a) and can be used for "bad" region identification. The angle of the filtered exponential field is shown in Fig. 12(c), which can be used for phase unwrapping. The phase is unwrapped only within "good" regions using flood algorithm [48]. The unwrapped phase is shown in Fig. 12(d), where "bad" regions are shown as black. One more example is shown in Fig. 13, where the phase map contains both "bad" pixels and regions.

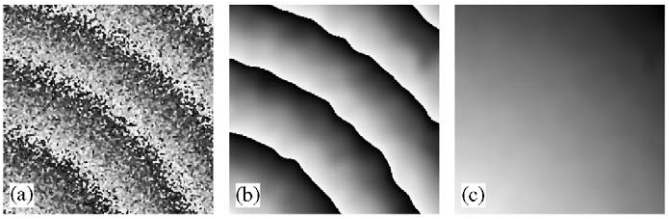

Fig. 11. Unwrap a phase map with "bad" pixels: (a) a wrapped phase; (b) wrapped phase filtered by WFF and (c) unwrapped phase of (b). Reprint from Ref. [50] with permission from Elsevier.

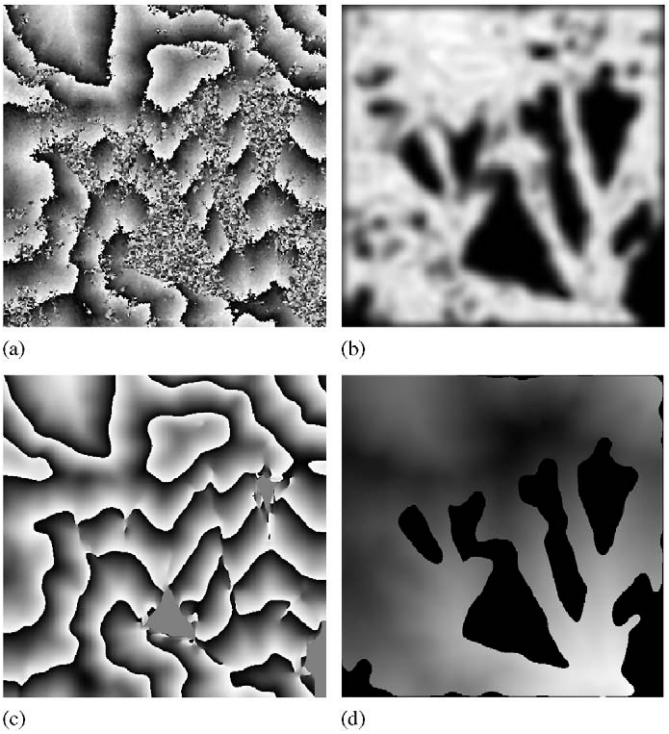

Fig. 12. Unwrap a phase map with "bad" regions: (a) wrapped phase map; (b) amplitude of filtered exponential field; (c) angle of filtered exponential field and (d) phase unwrapping only within "good" regions. Note that (a) is from synthetic aperture radar (SAR), not from an optical interferometer, but the phase unwrapping problem is the same. Data of (a) is from [48] with permission from John Wiley and Sons, Inc.

3.4. Phase-shifter calibration

In optical interferometry, it is often required to determine the phase-shift from two consecutive interferometric fringe patterns. For example, a phase-shifter has to be calibrated to get the relationship between the input of the phase-shifter and the resulting phase-shift between the consecutive fringe patterns [1]. Another example is in "generalized phase-shifting interferometry" where the phase-shifts are arbitrary and need to be determined before phase extraction can proceed [51,52]. One approach uses phase-shifting technique [53]. Using phase-shifting technique before phase-shifter calibration is somewhat awkward. Another approach uses carrier technique with Fourier

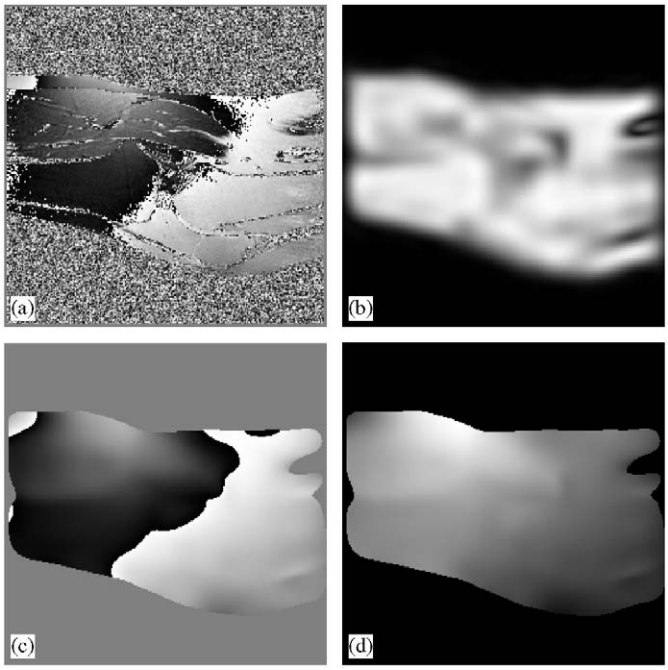

Fig. 13. Unwrap a phase map with "bad" pixels and regions: (a) wrapped phase map; (b) amplitude of filtered exponential field; (c) angle of filtered exponential field and (d) phase unwrapping only within "good" regions. Note that (a) is from magnetic resonance imaging (MRI), not from an optical interferometer, but the phase unwrapping problem is the same. Data of (a) is from [48] with permission from John Wiley and Sons, Inc.

transform [54]. However, it is generally too restrictive to enforce a carrier in the phase-shifted fringe patterns.

Though, generally, there is no carrier in a fringe pattern, it is reasonable to expect that it contains "carrier-like" features in some parts of fringe patterns. As indicated in notation (3) in Section 3.1, the phase and local frequencies extracted by WFR are accurate where the local frequencies are high. Hence, the phase-shift can be determined only from these "good" parts as follows [55],

(1) Given two phase-shifted fringe patterns, f_1 and f_2, apply WFR to obtain their respective phase and local frequencies as $\varphi_1(u,v)$, $\omega_{x1}(u,v)$, $\omega_{y1}(u,v)$, $\varphi_2(u,v)$, $\omega_{x2}(u,v)$ and $\omega_{y2}(u,v)$.
(2) Find the locations S where $\omega_1(u,v) = \sqrt{\omega_{x1}^2(u,v) + \omega_{y1}^2(u,v)}$ is large. The image boarders are excluded, as mentioned in notation (4) in Section 3.1.
(3) Phase-shift can be determined by computing in S the average value of

$$\Delta(u,v) = |\varphi_2(u,v) - \varphi_1(u,v)|. \tag{21}$$

It was mentioned in Section 2.3 that the phase by WFR should be corrected due to the second-order phase derivatives. However, $\varphi_1(u,v)$ and $\varphi_2(u,v)$ share the same second derivatives, this correction is unnecessary since they will be eliminated in Eq. (21).

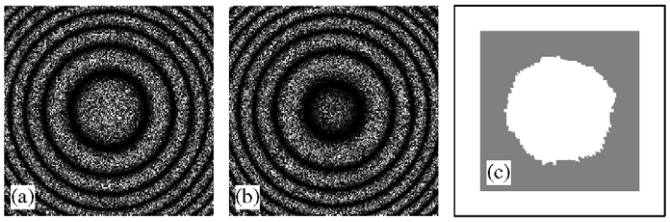

Fig. 14. phase-shift determination by WFR: (a) and (b), two phase-shifted fringe patterns and (c) location of "good" parts shown in gray.

As an example, two closed fringe patterns with a phase-shift of $\pi/2$ are simulated and shown in Figs. 14(a) and (b), respectively. The location for phase-shift determination can be found and is shown in Fig. 14(c). The phase-shift error is less than 0.01° for noiseless fringe patterns and is less than 1° for speckle fringe patterns of Figs. 14(a) and (b).

3.5. Fault detection

Detection of faults from interferometric fringe patterns is useful for condition monitoring, industrial inspection, nondestructive testing and evaluation (NDT and NDE) [56–59]. A fault occurs at location where the phase of the fringe changes abruptly. Accordingly there is a sudden change in the fringe density, or local frequencies, at that location. In the previous work [56–59], faults are detected from a single fringe pattern, though sequences of dynamic fringe patterns are often available [56]. In real applications, such as condition monitoring, a fringe sequence evolving over time is generally used to monitor the damages or faults. Moreover, the appearances of faults are very complicated. For example, different carrier frequencies give rise to different fault appearance, although the faults are the same. Hence it would be reasonable to monitor the temporal changes of the local frequencies. This can be realized by WFR as follows [60]:

(1) From the first fringe pattern f_1, extract local frequencies $\omega_{x1}(u,v)$ and $\omega_{y1}(u,v)$ using Eq. (15). The ridge value $r_1(u,v)$ can be recorded using Eq. (16) as

$$r_1(u,v) = |Sf_1[u,v,\omega_{x1}(u,v),\omega_{y1}(u,v)]|, \tag{22}$$

where $Sf_1(u,v,\xi,\eta)$ is the WFT spectrum of f_1. This means that the first fringe pattern in a local area around pixel (u,v) is most similar to WFT element $g_{u,v,\omega_x(u,v),\omega_y(u,v)}(x,y)$, with $r_1(u,v)$ as its similarity measure.
(2) Compute the similarity between the second fringe pattern f_2 in the local area around pixel (u,v) and the WFT element $g_{u,v,\omega_x(u,v),\omega_y(u,v)}(x,y)$ as

$$r_2(u,v) = |Sf_2[u,v,\omega_{x1}(u,v),\omega_{y1}(u,v)]|, \tag{23}$$

where $Sf_2(u,v,\xi,\eta)$ is WFT spectrum of f_2.
(3) If the value of $r_2(u,v)/r_1(u,v)$ decreases below a certain threshold, a fault is likely to occur at (u,v) since the similarity between f_1 and f_2 around (u,v) is low.

The effectiveness of this approach was analyzed theoretically in Ref. [60]. A simulated example and a real example are given in Figs. 15 and 16, respectively. The defective regions are successfully detected and highlighted with higher gray levels.

3.6. Edge detection and fringe segmentation

Till now it is assumed that the processed fringe has a continuous phase field, which is not always correct. For example, discontinuities exist when the tested objects, such as MEMS devices, have different components. Typical edge detectors, such as Canny edge detector [61], were developed for intensity discontinuities and are not suitable for phase discontinuities. As an example, Canny edge detector is applied to the fringe pattern in Fig. 17(a). The detected edges are overlaid on the original fringe pattern and shown in Fig. 17(b), which is obviously not satisfactory. Hence there is a need to handle the discontinuous phase field, which has been investigated using Gabor filters [43], Gabor wavelet [44,62] and Wigner–Ville distribution [63]. Gabor wavelet treats high and low frequencies unequally [62] and complex preprocessing is necessary to assist Wigner–Ville distribution [63]. Similar to Gabor filters [43], WFR can be used to detect the discontinuities simply and effectively for fringe patterns.

To detect the fringe edges caused by frequency discontinuities, the local frequencies $\omega_x(x,y)$ and $\omega_y(x,y)$ is calculated first using WFR. Then Canny edge detector is applied to either ω_x, ω_y, or $\omega=\sqrt{\omega_x^2+\omega_y^2}$ to locate the edges. Alternatively, ω and $\theta=\tan^{-1}(\omega_y/\omega_x)$ can also be used. Examples of some basic fringe patterns are shown in Figs. 18(a), (b), (d) and (e), where discontinuities of ω_x or ω_y are simulated. The detected edges are overlaid on the original fringe patterns. For fringe edges caused by phase discontinuities, high-frequency components appear due to these discontinuities and consequently regions around the edges can be isolated by thresholding the local frequencies. The edges can be found by thinning the isolated regions. Figs. 18(c) and (f) are two examples with a simulated phase-shift of $\pi/2$ in the right half of the fringe patterns. The detected edges are overlaid on the original fringe patterns. In the same manner, the fringe segmentation can also be realized. Fig. 19(a) shows a fringe pattern obtained using a Mach-Zender interferometer for measuring the refractive index of solution, where a potassium chloride (KCl) crystal is dissolved [64]. The fringes are segmented by retaining the regions where local frequencies are high (Fig. 19(b)).

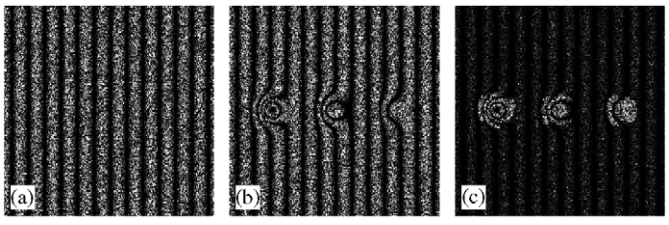

Fig. 15. Fault detection in simulated fringe patterns: (a) frame 1; (b)frame 2 and (c) fault alert in frame 2. Reprint from Ref. [60] with permission from Institute of Physics (IOP).

4. Implementations of WFF and WFR

Implementation issues are addressed in this section so that the results in this paper are reproducible and the algorithms can be readily tested by the readers [65]. Define

$$h_{\xi,\eta}(x,y)=g_{0,0,\xi,\eta}(x,y)=g(x,y)\exp(\mathrm{j}\xi x+\mathrm{j}\eta y), \tag{24}$$

it is easy to rewrite the important equations in Section 2 equivalently as follows:

$$Sf(u,v,\xi,\eta)=[f(u,v)\otimes h_{\xi,\eta}(u,v)]\exp(-\mathrm{j}\xi u-\mathrm{j}\eta v), \tag{9'}$$

$$f(x,y)=\frac{1}{4\pi^2}\int_{-\infty}^{\infty}\int_{-\infty}^{\infty}[f(x,y)\otimes h_{\xi,\eta}(x,y)]\otimes h_{\xi,\eta}(x,y)\,\mathrm{d}\xi\,\mathrm{d}\eta, \tag{10'}$$

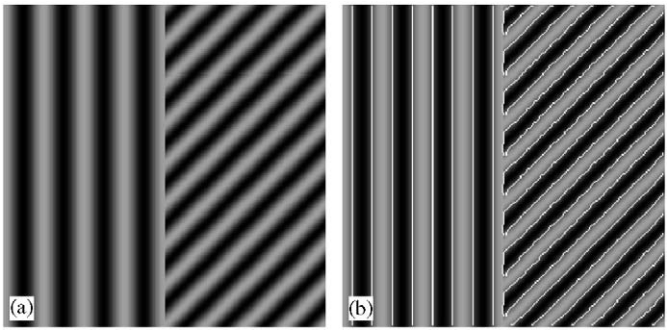

Fig. 17. A fringe pattern (a) and its intensity edges (b).

Fig. 16. Fault detection in real fringe patterns: (a) frame 1; (b)frame 2 and (c) fault alert in frame 2. Reprint from Ref. [60] with permission from Institute of Physics (IOP).

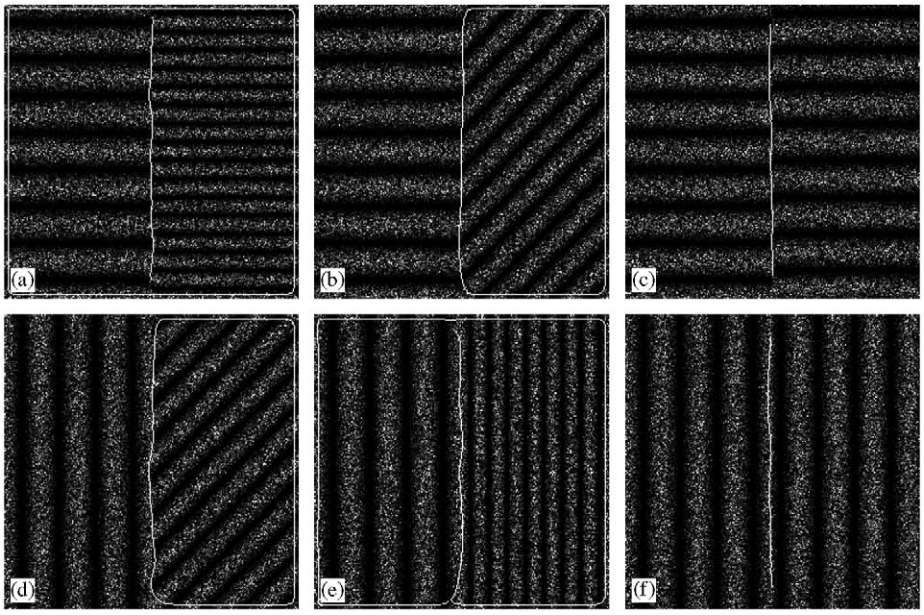

Fig. 18. Discontinuity detection in some basic fringe patterns.

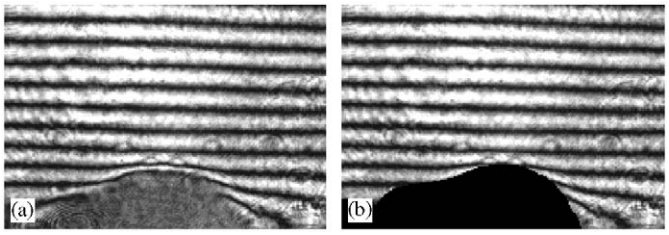

Fig. 19. A real fringe pattern with a crystal (a) and the segmented fringes (b).

$$\bar{f}(x,y)=\frac{1}{4\pi^2}\int_{\eta_l}^{\eta_h}\int_{\xi_l}^{\xi_h}\overline{[f(x,y)\otimes h_{\xi,\eta}(x,y)]}\otimes h_{\xi,\eta}(x,y)\,\mathrm{d}\xi\,\mathrm{d}\eta, \tag{13'}$$

$$[\omega_x(u,v),\omega_y(u,v)]=\arg\max_{\xi,\eta}|f(u,v)\otimes h_{\xi,\eta}(u,v)|, \tag{15'}$$

$$r(u,v)=|f(u,v)\otimes h_{\omega_x(u,v),\omega_y(u,v)}(u,v)|, \tag{16'}$$

$$\varphi(u,v)=\mathrm{angle}[f(u,v)\otimes h_{\omega_x(u,v),\omega_y(u,v)}(u,v)], \tag{17'}$$

where the symbol $\otimes$ denotes a 2-D continuous convolution.

All the above equations are continuous and should be discretized for implementation with a computer. It is assumed that the input fringe pattern $f(x,y)$ has already been discretized into pixels when it was captured by a CCD camera and consequently x and y here are integers. Accordingly x and y in $h_{\xi,\eta}(x,y)$ are also assumed to be integers and the unit of x and y is pixel. Now the symbol $\otimes$ should be understood as a 2-D discrete convolution. Finally, ξ and η should also be discretized, which can be simply done as follows:

$$\xi=p\xi_0,\quad p=\xi_l/\xi_0,\ldots,-1,0,1,\ldots,\xi_h/\xi_0\,, \tag{25}$$

$$\eta=q\eta_0,\quad q=\eta_l/\eta_0,\ldots,-1,0,1,\ldots,\eta_h/\eta_0\,, \tag{26}$$

where ξ_0 and η_0 are sampling intervals; p and q are integers. For WFF, it is shown by frame theory that $\xi_0=1/\sigma_x$ and $\eta_0=1/\sigma_y$ are recommended [41], while for WFR, ξ_0 and η_0 should be selected according to the desired frequency resolution and usually high resolution is preferred. Thus WFF is usually faster than WFR. Note that after discretization, the frequency range of $[\xi,\eta]$ must belong to $[-\pi,\pi]\times[-\pi,\pi]$, instead of $[-\infty,\infty]\times[-\infty,\infty]$ [30,31].

Two algorithms of WFF and WFR are integrated into a MATLAB® function `'wft2'`, which is provided in Fig. 20 and is used to produce all the results in this paper. The codes are also available on request. The input and output arguments are as follows,

- `type` means the algorithm to be used. Choose `'wff'` for WFF and `'wfr'` for WFR, respectively;
- `f` is an input fringe pattern. It can be f_I, f_{III} and f_{IV}. f_{II} is converted to f_I as input;
- `sigma` corresponds to σ_x and σ_y for Gaussian window function and $\sigma_x=\sigma_y=10$ is recommended [41] ;
- `wxl`, `wxi` and `wxh` (resp., `wyl` , `wyi` and `wyh`) correspond to ξ_l, ξ_0 and ξ_h (resp., η_l, η_0 and η_h). The choice of ξ_l and ξ_h (resp., η_l and η_h) for WFF and WFR are explained in Sections 2.2 and 2.3, respectively. `wxi = wyi = 1/sigma` is recommended for WFF [41];
- `thr` is the threshold for WFF in Eq. (14), which is not needed for WFR;
- `g` is the output of the function. It is a 2-D matrix for WFF, while it is a structure for WFR with the local frequencies, phase and ridges stored in `g.wx`, `g.wy`, `g.phase` and `g.r`, respectively. Note that `g.phase` is the *phase from ridges* and has not been corrected.

Gaussian function is chosen as the window function. The window size of $(6\sigma_x+1)\times(6\sigma_y+1)$ should be

```
function g=wft2(type,f,sigma,wxl,wxi,wxh,wyl,wyi,wyh,thr)

s=round(2*sigma);
[y x]=meshgrid(-s:s,-s:s);
w=exp(-(x.*x+y.*y)/2/sigma/sigma);
w=w/sqrt(sum(sum(w.*w)));
if strcmp(type,'wff')
    g=f*0;
    for wyt=wyl:wyi:wyh
        for wxt=wxl:wxi:wxh
            wave=w.*exp(j*wxt*x+j*wyt*y);
            sf=conv2(f,wave,'same');
            sf=sf.*(abs(sf)>=thr);
            g=g+conv2(sf,wave,'same');
        end
    end
    g=g/4/pi/pi*wxi*wyi;
elseif strcmp(type,'wfr')
    g.wx=f*0;g.wy=f*0;g.phase=f*0;g.r=f*0;
    for wyt=wyl:wyi:wyh
        for wxt=wxl:wxi:wxh
            wave=w.*exp(j*wxt*x+j*wyt*y);
            sf=conv2(f,wave,'same');
            t=(abs(sf)>g.r);
            g.r=g.r.*(1-t)+abs(sf).*t;
            g.wx=g.wx.*(1-t)+wxt*t;
            g.wy=g.wy.*(1-t)+wyt*t;
            g.phase=g.phase.*(1-t)+angle(sf).*t;
        end
    end
end
```

Fig. 20. MATLAB® codes for 2-D WFT.

selected. To save computation time, it is assigned to be $(4\sigma_x+1)\times(4\sigma_y+1)$ in the codes since it gains 91.1% energy of the Gaussian function and less than 10% of energy is truncated. Users can adjust it by modifying the first line of codes to "`s = round(3*sigma);`" to expand the window size if computation time is not concerned.

As examples, fringes in Figs. 3 and 4 are obtained by executing the following commands in MATLAB® environment, respectively,

g = wft2('wff',f,10,-0.7,0.1,0.7,-0.7,0.1,0.7,6);
g = wft2('wfr',f,10,0,0.025,0.5,-0.5,0.025,0.5).

About 2 and 9 min are taken to execute the above commands for a fringe pattern of 256×256 by a Pentium IV 3.2 GHz desktop.

It can be noted that the 2-D WFT kernel is separable and can be written as the production of two 1-D kernels:

$$g_{u,v,\xi,\eta}(x,y)=g_{u,\xi}(x)g_{v,\eta}(y) \tag{27}$$

with

$$g_{u,\xi}(x)=\exp(-x^2/2\sigma_x^2+\mathrm{j}\xi x), \tag{28}$$

$$g_{v,\eta}(y)=\exp(-x^2/2\sigma_y^2+\mathrm{j}\eta y). \tag{29}$$

Thus the 2-D convolution can be realized by a 1-D convolution along each row, followed by a 1-D convolution along each column. This is similar to the realization of

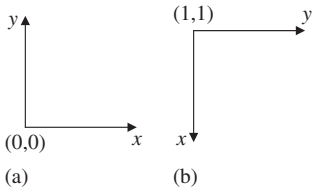

Fig. 21. Coordinate systems for theoretical analysis (a) and for MATLAB® (b).

2-D FFT by two 1-D FFTs [31]. By this modification, the execution time of the previous examples reduces to 45 s and 3 min, respectively.

Finally it should be noted that, in Sections 1 and 2, it is comfortable to assume the coordinate system as in Fig. 21(a), while in the MATLAB® codes, it is assumed that the coordinate system is as in Fig. 21(b), which follows the convention of MATLAB®.

5. Conclusions

Demodulation of fringe patterns is necessary for many optical metrological systems. Systematic solutions using time–frequency analysis are provided. Two-dimensional windowed Fourier transform is chosen for the determination of phase and phase derivatives and it is compared with other time–frequency techniques. Two approaches are developed, one is based on the concept of filtering the fringe pattern and the other is based on the similarity measure between the fringe pattern and windowed Fourier elements. Their applications in determination of phase and phase derivatives, strain extraction in moiré interferometry, phase unwrapping, phase-shifter calibration, fault detection and edge detection and fringe segmentation are given, showing that windowed Fourier transform is a very useful technique for various fringe pattern analysis tasks. Finally, how to implement the algorithms is discussed so that readers can easily reproduce the results and use these techniques to solve their own problems.

Acknowledgments

I would like to express my sincere gratitude to Prof. Seah Hock Soon and Prof. Anand Asundi of the Nanyang Technological University and Prof. Wu Xiaoping of the University of Science and Technology of China for their encouragement and to the reviewers for their helpful comments.

References

[1] Robinson DW, Reid GT, editors. Interferogram analysis: digital fringe pattern measurement techniques. Bristol, England: Institute of Physics; 1993.
[2] Huntley JM. Automated fringe pattern analysis in experimental mechanics: a review. J Strain Anal 1998;33:105–25.
[3] Dorrio BV, Fernandez JL. Phase-evaluation methods in whole-field optical measurement techniques. Meas Sci Technol 1999;10:R33–55.

[4] Servin M, Kujawinska M. Modern fringe analysis in interferometry. In: Malacara D, Thompson BJ, editors. Handbook of optical engineering. New York: Marcel Dekker; 2001.
[5] Creath K. Phase-measurement interferometry techniques. In: Wolf E, editor. Progress in optics, vol. 26. Amsterdam: Elsevier; 1988. p. 349–93.
[6] Takeda M, Ina H, Kobayashi S. Fourier transform methods of fringe-pattern analysis for computer-based topography and interferometry. J Opt Soc Am 1982;72:156–60.
[7] Kemao Q, Soon SH, Asundi A. Smoothing filters in phase-shifting interferometry. Opt Laser Technol 2003;35:649–54.
[8] Servin M, Marroguin JL, Cuevas FJ. Demodulation of a single interferogram by use of a two-dimensional regularized phase-tracking technique. Appl Opt 1997;36:4540–8.
[9] Servin M, Rodriguez-Vera R, Marroquin JL, Malacara D. Phase-shifting interferometry using a two-dimensional regularized phase-tracking technique. J Mod Opt 1998;45:1809–19.
[10] Servin M, Cuevas FJ, Malacara D, Marroguin JL, Rodriguez-Vera R. Phase unwrapping through demodulation by use of the regularized phase-tracking technique. Appl Opt 1999;38:1934–41.
[11] Villa J, Servin M. Robust profilometer for the measurement of 3-D object shapes based on a regularized phase tracker. Opt Laser Eng 1999;31:279–88.
[12] Servin M, Marroquin JL, Cuevas FJ. Fringe-follower regularized phase tracker for demodulation of closed-fringe interferograms. J Opt Soc Am A 2001;18:689–95.
[13] Watkins LR, Tan SM, Barnes TH. Determination of interferometer phase distributions by use of wavelets. Opt Lett 1999;24:905–7.
[14] Fang J, Xiong CY, Li HJ, Zhang ZL. Digital transform processing of carrier fringe patterns from speckle-shearing interferometry. J Mod Opt 2001;48:507–20.
[15] Liu H, Cartwright AN, Basaran C. Sensitivity improvement in phase-shifted moiré interferometry using 1-D continuous wavelet transform image processing. Opt Eng 2003;42:2646–52.
[16] Liu H, Cartwright AN, Basaran C. Moiré interferogram phase extraction: a ridge detection algorithm for continuous wavelet transforms. Appl Opt 2004;43:850–7.
[17] Kadooka K, Kunoo K, Uda N, Ono K, Nagayasu T. Strain analysis for moiré interferometry using the two-dimensional continuous wavelet transform. Exp Mech 2003;43:45–51.
[18] Qian K, Seah HS, Asundi A. Instantaneous frequency and its application in strain extraction in moiré interferometry. Appl Opt 2003;42:6504–13.
[19] Sciammarella CA, Kim T. Determination of strains from fringe patterns using space–frequency representations. Opt Eng 2003;42:3182–93.
[20] Dursun A, Ozdar S, Ecevit FN. Continuous wavelet transform analysis of projected fringe patterns. Meas Sci Technol 2004;15:1768–72.
[21] Zhong J, Weng J. Spatial carrier-fringe pattern analysis by means of wavelet transform: wavelet transform profilometry. Appl Opt 2004;43:4993–8.
[22] Tay CJ, Quan C, Fu Y, Huang Y. Instantaneous velocity displacement and contour measurement by use of shadow moiré and temporal wavelet analysis. Appl Opt 2004;43:4164–71.
[23] Fu Y, Tay CJ, Quan C, Miao H. Wavelet analysis of speckle patterns with a temporal carrier. Appl Opt 2005;44:959–65.
[24] Federico A, Kaufmann GH. Phase retrieval in digital speckle pattern interferometry by use of a smoothed space–frequency distribution. Appl Opt 2003;42:7066–71.
[25] Qian K. Windowed Fourier transform for fringe pattern analysis. Appl Opt 2004;43:2695–702.
[26] Qian K. Windowed Fourier transform for fringe pattern analysis: addendum. Appl Opt 2004;43:3472–3.
[27] Qian K, Seah HS, Asundi A. Filtering the complex field in phase shifting interferometry. Opt Eng 2003;42:2792–3.
[28] Larkin KG, Bone DJ, Oldfield MA. Natural demodulation of two-dimensional fringe patters, I: general background of the spiral phase quadrature transform. J Opt Soc Am A 2001;18:1862–70.
[29] Mallat S. A wavelet tour of signal processing. 2nd ed. San Diego: Academic Press; 1999.
[30] Oppenheim AV, Schafer RW, Buck JR. Discrete-time signal processing. 2nd ed. Englewood Cliffs, NJ: Prentice-Hall; 1999.
[31] Gonzalez RC, Woods RE. Digital image processing. 2nd ed. Englewood Cliffs, NJ: Prentice-Hall; 2002.
[32] Qian S. Introduction to time-frequency and wavelet transform. Englewood Cliffs, NJ: Prentice-Hall, PTR; 2002.
[33] Qian K. Windowed Fourier transform for demodulation of carrier fringe patterns. Opt Eng 2004;43:1472–3.
[34] Kreis T. Digital holographic interference-phase measurement using the Fourier transform method. J Opt Soc Am A 1986;3:847–55.
[35] Qian K, Seah HS, Asundi AK. Algorithm for directly retrieving the phase difference: a generalization. Opt Eng 2003;42:1721–4.
[36] Delprat N, Escudié B, Guillemain P, Kronland-Martinet R, Tchamitchian P, Torrésani B. Asymptotic wavelet and Gabor analysis: extraction of instantaneous frequencies. IEEE Trans Inf Theory 1992;38:644–64.
[37] Guillemain P, Kronland-Martinet R. Characterization of acoustic signals through continuous linear time–frequency representations. Proc IEEE 1996;84:561–85.
[38] Kaufmann GH, Galizzi GE. Speckle noise reduction in television holography fringes using wavelet thresholding. Opt Eng 1996;35:9–14.
[39] Federico A, Kaufmann GH. Comparative study of wavelet thresholding methods for denoising electronic speckle pattern interferometry fringes. Opt Eng 2001;40:2598–604.
[40] Teolis A. Computational signal processing with wavelets. Boston: Birkhäuser; 1998.
[41] Qian K, Soon SH. Two-dimensional windowed Fourier frames for noise reduction in fringe pattern analysis. Opt Eng 2005;44:075601.
[42] Laine AF. Wavelets in temporal and spatial processing of biomedical images. Annu Rev Biomed Eng 2000;2:511–50.
[43] Bovik AC, Clark M, Geisler WS. Multichannel texture analysis using localized spatial filters. IEEE Trans Pattern Anal Mach Intell 1990;12:55–73.
[44] Bovik AC, Gopal N, Emmoth T, Restrepo A. Localized measurement of emergent image frequencies by Gabor wavelets. IEEE Trans Inf Theory 1992;38:691–712.
[45] Rivera M. Robust phase demodulation of interferograms with open or closed fringes. J Opt Soc Am A 2005;22:1170–5.
[46] Quan C, Tay CJ, Yang F, He X. Phase extraction from a single fringe pattern based on guidance of an extreme map. Appl Opt 2005;44:4814–21.
[47] Asundi A, Cheung MT. Moiré of moiré interferometry. Exp Tech 1987;11(8):28–30.
[48] Ghiglia DC, Pritt MD. Two-dimensional phase unwrapping: theory, algorithm and software. New York: Wiley; 1998.
[49] Itoh K. Analysis of the phase unwrapping algorithm. Appl Opt 1982;21:2470.
[50] Qian K, Soon SH, Asundi A. A simple phase unwrapping approach based on filtering by windowed Fourier transform. Opt Laser Technol 2005;37:458–62.
[51] Cai LZ, Liu Q, Yang XL, WAng YR. Phase-shift extraction and wave-front reconstruction in phase-shifting interferometry with arbitrary phase steps. Opt Lett 2003;28:1808–10.
[52] Cai LZ, Liu Q, Yang XL. Generalized phase-shifting interferometry with arbitrary unknown phase steps for diffraction objects. Opt Lett 2004;29:183–5.
[53] Gutmann B, Weber H. Phase-shifter calibration and error detection in phase-shifting applications: a new method. Appl Opt 1998;37:7624–31.
[54] Goldberg KA, Bokor J. Fourier-transform method of phase-shift determination. Appl Opt 2001;40:2886–94.

[55] Qian K, Soon SH, Asundi A. Calibration of phase-shift from two fringe patterns. Meas Sci Technol 2004;15:2142–4.
[56] Osten W, Juptner W, Mieth U. Knowledge assisted evaluation of fringe patterns for automatic fault detection. In: Pryputniewicz RJ, Brown GM, Juptner WP, editors. Interferometry VI: applications; Proc SPIE 1993;2004:256–68.
[57] Juptner W, Mieth U, Osten W. Application of neural networks and knowledge based systems for automatic identification of fault indicating fringe patterns. In: Pryputniewicz RJ, Stupnicki J, editors. Interferometry '94; Proc SPIE 1994;2342:16–26.
[58] Li X. Wavelet transform for detection of partial fringe patterns induced by defects in nondestructive testing of holographic interferometry and electronic speckle pattern interferometry. Opt Eng 2000;39:2821–7.
[59] Krüger S, Wernicke G, Osten W, Kayser D, Demoli N, Gruber H. Fault detection and feature analysis in interferometrer fringe patterns by the application of wavelet filters in convolution processors. J Electron Imag 2001;10:228–33.
[60] Qian K, Seah HS, Asundi A. Fault detection by interferometric fringe pattern analysis using windowed Fourier transform. Meas Sci Technol 2005;16:1582–7.
[61] Canny J. A computational approach to edge detection. IEEE Trans Pattern Anal Mach Intell 1986;8:679–98.
[62] Hongbin Z, Qing W. Measuring instantaneous frequencies of fringe image and its application in phase unwrapping. Acta Electron Sinica 1999;27:15–8.
[63] Federico A, Kaufmann GH. Retrieval of phase-derivative discontinuities in digital speckle pattern interferometry fringes using the Wigner–Ville distribution. In: Creath K, Schmit J, editors. Interferometry XII: techniques and analysis; Proc SPIE 2004;5531:127–33.
[64] Miao H. The studies on real time phase measurement technique and its application to protein crystal growth, PhD dissertation, University of Science and Technology of China, PR China, 1999.
[65] Buckheit J, Donoho DL. Wavelab and reproducible research. In: Antoniadis A, Oppenheim G, editors. Wavelets and statistics. New York: Springer; 1995. p. 55–82.